INTEGRATION OF A CHROMATIC ABERRATION TECHNIQUE FOR IN SITU WORKING DISTANCE MEASUREMENT DURING POWDER BLOWN LASER DIRECTED ENERGY DEPOSITION ADDITIVE MANUFACTURING

A Dissertation
Presented to
The Academic Faculty

by

Matteo Venturiello

In Partial Fulfillment
of the Requirements for the Degree
Master of Science in the
George W. Woodruff School of Mechanical Engineering

Georgia Institute of Technology
[August 2025]

INTEGRATION OF A CHROMATIC ABERRATION TECHNIQUE FOR IN SITU WORKING DISTANCE MEASUREMENT DURING POWDER BLOWN LASER DIRECTED ENERGY DEPOSITION ADDITIVE MANUFACTURING

Approved by:

Dr. Aaron Stebner, Advisor
School of Mechanical Engineering
Georgia Institute of Technology

Dr. Jin Yeon Kim
School of Mechanical Engineering
Georgia Institute of Technology

Dr. Carolyn C Seepersad
School of Mechanical Engineering
Georgia Institute of Technology

Date Approved: [July 23 2025]

ACKNOWLEDGEMENTS

I want to thank my family, my friends and my girlfriend Eleonora that have always supported me during this time.

I want to thank my advisor Professor Aaron Stebner for the opportunity to develop this research project under his supervision.

I want to thank also Professor Jin Yeon Kim and Professor Carolyn Seepersad for being part of the Graduate Committee and for their important feedback on this project.

Special thanks to The Beam Team, especially Dr. Zachary Brunson, for the time we spent together and the willingness to always discuss and collaborate.

Finally, I want to thank all the faculty and staff of the Artificial Intelligence Manufacturing Pilot Facility (AI-MPF) for their guidance and technical support during this period.

TABLE OF CONTENTS

ACKNOWLEDGEMENTS **iv**

LIST OF TABLES **vii**

LIST OF FIGURES **viii**

LIST OF SYMBOLS AND ABBREVIATIONS **ix**

SUMMARY **x**

CHAPTER 1 Introduction **1**
1.1 Motivation **1**
1.1.1 Directed energy deposition 1
1.1.2 Working distance monitoring 2
1.2 Literature review **3**
1.2.1 Predictive model-based approaches 3
1.2.2 In-situ monitoring 4
1.2.3 Chromatic aberration technique 5

CHAPTER 2 Materials and methods **8**
1.3 Optomec LENS MTS 860 **8**
1.3.1 Optical description 8
1.3.2 Metal powder 10
1.3.3 Printing parameters 11
1.4 Keyence VR-6000 **11**

CHAPTER 3 Sensor Hardware design **13**
1.5 Radiation acquisition optics **14**
1.5.1 Theory 14
1.5.2 Optical scheme 17
1.5.3 Acquisition optics elements 20
1.5.4 Hot mirror analysis 23
1.6 Processing optics **27**
1.6.1 Radiation theory 27
1.6.2 Components in processing optics 28
1.6.3 Radiation analysis 29
1.7 Design optimization **32**
1.7.1 Trial tests 32
1.7.2 Optimization setup and results 35
1.7.3 Discussion on other sources of errors 37
1.8 Final design **38**
1.8.1 Fiber optic cable 38
1.8.2 O-ring selection 39

1.8.3 Temperature safety 39

CHAPTER 4 Sensor performance 41
1.9 Test description 41
1.10 Stainless steel results 42
1.11 Aluminum results 45
1.12 Discussion on the results 48
1.13 Additional tests 49

CHAPTER 5 Conclusions and future work 51
1.14 Real time feedback control 51
1.15 Applicability in DED technology 52
1.16 Future work 53

REFERENCES 55

LIST OF TABLES

Table 1 Optomec focusing lens specification 9
Table 2 Fiber optic specification.. 21
Table 3 Bi-convex sensor lens 22
Table 4 Hot mirrors available online 25
Table 5 New combinantion of parameters for stainless steel tests 50
Table 6 New combinantion of paramters for aluminum tests................................. 50

LIST OF FIGURES

Figure 1 Example of under-building in DED (courtesy of Bhairav Ramanathan) . 3
Figure 2 Optical system in the Optomec® printing head 10
Figure 3 A schematic of the working distance measurement sensor 13
Figure 4 2-D laser beam representation scheme 14
Figure 5 Thin lens scheme 15
Figure 6 Snell's law 16
Figure 7 Sensor optical scheme 18
Figure 8 Radiation beam starting point.. 19
Figure 9 Fiber optic and NA 20
Figure 10 Lens selection 21
Figure 11 Refraction effect of hot mirror 24
Figure 12 Hot mirror scheme 26
Figure 13 Radiation spectrum for aluminum and steel. Ideal Plank's blackbody radiation is assumed at their melting temperature 28
Figure 14 Optical detection box scheme... 29
Figure 15 Theoretical radiation acquired by the sensor.. 30
Figure 16 Theoretical radiation acquired by the sensor (log scale)....................... 31
Figure 17 Optomec printing head on vertical support + first tests set-up............. 33
Figure 18 Sensor signa from the test with a flashlight... 34
Figure 19 Sensor signa from the test with hot steel 34
Figure 20 Optimization set-up 35
Figure 21 $\boldsymbol{Z2}$ optimal value 36
Figure 22 Transverse adjustment.. 37
Figure 23 Final design 40
Figure 24 Visible and IR signals acquired during a test with stainless steel 42
Figure 25 Visible voltage values plotted with respect to the working distance.... 44
Figure 26 Calibration curve for stainless steel... 45
Figure 27 Data acquired during a test with aluminum... 46
Figure 28 Average visible voltage levels plotted with respect to the working distance 47
Figure 29 Calibration curve for aluminum 48

LIST OF SYMBOLS AND ABBREVIATIONS

Vis	Visible spectral band (400-450 nm)
IR	Infrared spectral band (800-1200 nm)
T_{avg}	Average transmission rate
R_{avg}	Average reflection rate

SUMMARY

Powder blown laser Directed Energy Deposition (DED) is an additive manufacturing process that is increasingly being adopted in industry for its capability of realizing complex parts with several metal alloys. However, because of the nature of the process, the height of the deposited material can slightly deviate from the intended height, which affects the working distance (the distance between the deposition nozzle and the material deposited). This issue leads to inconsistency in deposited layer thickness and also to inferior mechanical properties. Such errors, if being accumulated, can generate significant discrepancies between the desired model and the printed object, resulting in a waste of time and material. Therefore, controlling the working distance is critical in optimizing the process.

To address this issue, this research develops a sensor that can in-situ measure the working distance and can ultimately be used for real-time control of the DED process. The sensor takes the radiation from the molten metal in the melt pool as a light source, which eliminates the needs for any additional space-taking light sources. The sensing mechanism is based on the optical phenomenon called the chromatic aberration – wavelength-dependent focal distance.

A lens is added to the existing optical system inside the printing head to collect lights radiating from the melt pool which are then delivered to a detecting optics through a fiber optic cable. The detecting optical system filter and process the lights in two wavelength bands. Changing the working distance changes the focal lengths of these two

wavelength bands and accordingly their signal intensities. Therefore, these relative intensity changes are directly related to the changes in the working distance.

The sensor is calibrated for two different materials using a series of single-track prints; the heights of these single-tracks are then measured using a profilometer. Since the radiation spectrum depends on the temperature of the emitting surface; the calibration curve is unique to each material with its specific melting temperature. For this reason, two materials with very much different thermal and physical properties are tested. A steel alloy is chosen for its widespread industrial use, while an aluminum alloy is chosen to take advantage of the feature of the printer that allows to operate in a fully inert atmosphere. A procedure to process the acquired data and calibrate the sensor is proposed. The raw signal acquired is first cleaned from outliers that can negatively influence the measurement. Then, the resulting voltages (one for each wavelength band) are combined into a single-value error metric that directly correlates with a working distance. The results demonstrate that the developed sensor can precisely estimate the working distance and so be used as feedback control for the printing process. The sensor is completely passive, not requiring additional laser sources, and its sampling frequency is higher than those of existing camera-based techniques. Moreover, the sensor is designed as an add-on to the existing print head and does not interfere with the workspace of the DED system. Its compact design facilitates its applicability into powder-blown DED systems. Possible future work and optimization are also discussed.

CHAPTER 1 INTRODUCTION

1.1 Motivation

1.1.1 Directed energy deposition

Directed energy deposition (DED) is one of the seven categories of additive manufacturing technologies defined by ISO/ASTM 52900. In powder blown laser-based DED, a focused energy source is used to melt metal powder which is simultaneously blown and deposited by a nozzle. This process can create arbitrary shape on even and uneven substrates through line-by-line deposition. Like other additive manufacturing technologies, DED provides advantages over the conventional manufacturing technologies, including design freedom, rapid prototyping, scalability, and space efficiency. Most DED systems include multiple hoppers so they can realize successive or simultaneous deposition of powder and fabricate heterogeneous materials with desired properties. The process relies on several parameters such as laser beam shape, laser power, printing speed, and powder feed rate. All these parameters affect the performance of the final component. Bead formation, joining between successive layers, porosity, microstructure, and residual stresses are all dependant on these parameters. Usually, energy densities of the laser are on the order of 10^6 W/mm^2, typical layer thickness is 250-500 μm, minimum feature size is around 380-1000 μm and deposition rate 8.3 g/min [1]. The deposition rate and the volume density of DED processes are greater than those of the powder bed fusion (PBF) process, while layer thickness, surface roughness and minimum feature size of printed parts are relatively larger compared to PBF. DED has gained considerable interest in the manufacturing industry also for repair and remanufacturing of products as a potential alternative to the traditional welding processes. For example, hot sections, knife-edges, blades, and compressor seals have been repaired by DED processes to reduce costs and lead time [1].

1.1.2 Working distance monitoring

Process optimization is the primary issue in DED; more specifically in-situ monitoring and feedback control is one of the major research directions to enhance product quality and minimize material defects. The objective of this research is to develop an in-situ sensor that can detect the working distance during printing and eventually be used to build real-time feedback control based on the measured distance. Working distance, being defined as the distance between the laser source nozzle and the built surface, is usually set to be a constant process parameter for a given material at the beginning of each print. However, the printing process is characterized by multidimensional motions between the workpiece and the printing head and by local unpredictable interactions between the laser beam and powder being melt. These inevitably lead to variations of the layer height and consequently changes in working distance. In addition, changes in working distance affect laser focus modifying the powder flow and thus the layer height [2]. The variations of working distance make the laser less energy-efficient and thus can significantly reduce the build speed as shown in Figure 1 In contrast to PBF where a part's dimensional height accuracy is easily ensured by setting layer thickness as a function of the powder size [3], controlling layer thickness for good dimensional accuracy in DED is more difficult due to the unsteady mass flow rate. Being the print of each layer influenced by the previous layer is easy to cause errors accumulation and shape deviation from the original model in the design [4]; this phenomenon is also called underbuilt. The underbuilt could be so significant that the built parts become completely useless (see Figure 1). In addition, lack in uniform layer thickness is directly linked to a non-uniform microstructure [5] and a loss of mechanical properties in the component, especially toughness [6].

Figure 1 Example of under-building in DED (courtesy of Bhairav Ramanathan)

1.2 Literature review

In order to obtain real-time sensing of the working distance, the particular working conditions do not allow using contact sensor solutions. Previous research that has been done trying to evaluate the working distance, can be divided into two major categories.

1.2.1 Predictive model-based approaches

Several publications deal with the problem of controlling the working distance by building models that are capable of predicting the bead geometry and, consequently the layer height. These models are based on theoretical descriptions of the printing process and are validated through a series of experiments. One of the most common experimental methods is to print a series of single tracks using different printing parameters. Then, the section of each single track is analysed through optical microscopy to acquire bead geometry data for the model [7]. Haley et al. [8] demonstrate that, with the developed model and a passive self-regulating stability feedback loop, it is possible to make the working distance converge to a desired value. Another approach involves a machine learning model trained with melt pool images [2], which can also predict the optimal working distance during the pre-build stage. Although these models can be very reliable, they are effective within selected boundary parameters (material, printing speed, laser power, etc.), whenever those parameters change, a new model needs to be developed or trained, which seems to be impractical.

1.2.2 In-situ monitoring

There have also been attempts to build sensors capable of measuring the printing distance in real time. Some of them use imaging techniques [9], where the melt pool height is monitored by three high speed charged couple device (CCD) cameras in a triangulation setup.

Techniques such as in-line coherent imaging give the possibility to map the surface being printed and to investigate the effects of the humping geometry [10]. This solution allows taking measurements on the melt pool without interfering with the printing laser, the entire sensor setup being placed at an angle with respect to the vertical printing axis. In some systems, a laser scanner is attached to the printing head [11], which scans the bead after solidification following the printing direction of the head, then build height and other data are extracted from the scan. Unfortunately, this method is not useful to get real time height data but just to check the profile only after the layer has already been printed. Other sensors employ in-line, non-contact laser techniques to detect the working distance based on a coaxial laser triangulation [12]. Moreover, there are manufacturing systems such as laser welding where working distance sensors based on low coherence interferometry is adopted [13] and because of the similarities between the two processes, it is possible to integrate the technique also in DED [14]. It is interesting to notice that in these set-ups the printing laser and the sensor laser travel along the same path to reach the melt pool, so all the designs have some type of mirror to separate the two lasers. Note that this is possible because printing laser and sensor laser have different frequencies. The laser separation makes the sensor source and receiver to be at different positions with respect to the printing laser source. All these laser techniques have some common issues. While the source laser sends signals towards the target location intended to measure the depth, the reflection comes from somewhere else than the intended location. This system is poorly compatible with the DED process, where the melt pool acts as a source of scattering that could possibly make the measurement process to be difficult. Moreover, radiation sources such as the printing laser and the melt pool could interfere with the measurement laser lights and introduce error sources.

1.2.3 Chromatic aberration technique

The technique known as the chromatic aberration technique [15] could make the sensor easy to implement by eliminating the need of a source laser and taking advantage of the radiation generated by the melt pool. This technique does not require a separate laser source or a receiver but requires a lens and a fiber optic cable. The lens is used to focus the radiation from the melt pool inside a fiber optic cable. Variations in the working distance will change the amount of radiation delivered inside the fiber optic. The incoming radiation is transmitted through the fiber optic into an optical detection box. Here intensities in two spectral bands are detected: one in the visible/UV range (V_{Vis}) and one in the infrared (V_{IR}) and then through a simple weighted subtraction, it is possible to obtain a unique number, error signal (ε), that is directly correlated with the working distance (Eq.1).

$$\varepsilon = V_{Vis}G_{Vis} - V_{IR}G_{IR} \qquad \text{(Eq.1)}$$

Here, the two gain values (G_{Vis} and G_{IR}) are used to adjust the intensities detected and let both terms in (Eq.1) be in the same order of magnitude. Because the different wavelengths focus at different focal distances, the intensity percentage change of each spectral band is different. The signal detected is first low-pass filtered to remove high frequency intensity modulation generated by the melt pool oscillation.

Similar solutions have been explored trying to implement optical sensors based on the phenomenon of the chromatic aberration. Ćwikła et al. [16] proposes a method where an additional laser source is combined with an acquisition system which is designed to increase the effect of the chromatic aberration. Some numerical simulation and preliminary experimental results are presented. The proposed method is still an active system that requires a laser source and the overall optical system is more complex than the one proposed by Hand et al. [15]. Herberger et al. [17] developed a system that is using chromatic aberration with three different colours (RGB) acquiring the data using a camera. The use of multiple colours increases the accuracy of the system and there are no active laser sources in their setup, making the system completely passive. A study about the best algorithm to process the two-dimensional pixel data has been done, together with some tests on the sensor accuracy. However, the sampling rate of the camera is limited, creating potential issues in its implementation as real time sensor for feedback control.

CHAPTER 2 MATERIALS AND METHODS

1.3 Optomec LENS MTS 860

Optomec® is a hybrid manufacturing machine that integrates laser engineered net shaping (LENS), DED technology, and traditional subtractive manufacturing techniques to build repair and coat metal components. LENS technology uses computer-controlled lasers that weld air-blown streams of metallic powders through nozzles into custom parts and manufacturing molds. One of the purposes of LENS is to make small lots of high-density parts or molds. Nozzles each direct a stream of metal powder at a central point beneath them. Simultaneously, that point is heated by a high-power, focused laser beam. The laser and powder jets remain stationary while the model and its substrate are moved to provide new targets on which to deposit metal continually. Optomec® uses a YAG laser source to melt metal powders; the entire process is realized inside a sealed Argon atmosphere that allows to work with various alloys without the risk of oxidation.

1.3.1 Optical description

For the scope of this research, it is important to analyse and understand the Optomec® machine from an optical point of view, to determine the optimal location for the sensor to be developed and all the optical elements that are going to interact with it. It is evident that, the best way to install the working distance sensor is to be integrated within the printing head. In this way, the sensor can automatically and accurately follow the motion of the printing head without introducing any additional relative motion. In the printing head, the purpose of the optical elements is to control and drive the melting laser beam from its source (guided through a fiber optic cable) to the nozzle and focusing it to melt the powder, as shown in Figure 2. The laser beam starts from the right of the printing head and thanks to two hot mirrors is reflected twice to reach the left side of the head. Here there is a lens (Table 1) that focuses the beam before it comes out of the nozzle through its central hole. The focused beam then reaches the printing surface. The internal optic path is completely shielded from the outside by a series of cover glasses at the terminal points. There is an additional cover glass on the top left of the printing head, providing a free optical channel meant to be used to place a camera sensor, that will be used by this research for in-situ measurements.

Table 1 Optomec focusing lens specification

Material	Focal length	Diameter	Additional features
Fused silica	200mm (at 1080nm)	1.10inch	Antireflecting coating on both sides

Other specifications regarding the optical elements inside the printing head are the manufacturer's proprietary and thus not shared.

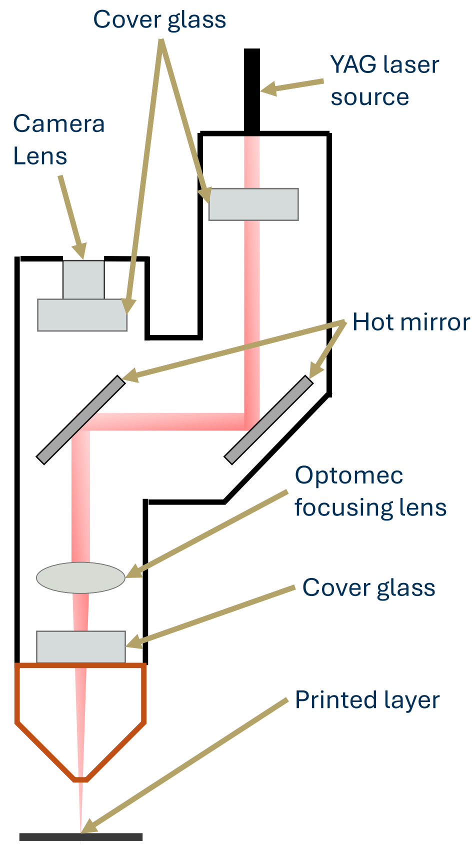

Figure 2 Optical system in the Optomec® printing head

1.3.2 Metal powder

Experiments are conducted using two alloy powders to validate the performance of the sensor with different materials. Among the large number of alloys available, 316 stainless steel and A1000-RAM10 are selected. Al1000-RAM10 is an aluminum alloy with titanium (Ti) and boron carbide (B_4C) added as pre ceramics. During the deposition, they react to create titanium carbide (TiC) and titanium diboride (TiB_2). These alloys belong to two categories, steel and aluminum, that are widely used in research trying to improve their printing performances [18, 19]. The importance of these alloys is that these are also widely used in industry for different applications. In addition, their behaviours in the printing process are quite different. For example, 316 stainless steel is an alloy that is relatively easy to print while aluminum, as shown in different research [18], exposes more problems in finding the optimal set of parameters for printing and reaching good deposition. Validating the sensor for these two different alloys will help ensure the performance and efficiency of the developed sensor.

1.3.3 Printing parameters

On the Optomec® printer there are 3 major parameters can be set during the print: laser power, printing speed, and powder feed rate. The laser power is indicated in Watts while the printing speed is indicated in inches per minute. The powder feed rate is controlled by setting the speed in rpm of a disk with holes inside the hopper that is containing the powder. When the disk is rotating, the powder drops through the holes and enters an Argon flow to reach the nozzle and get deposited, therefore increasing the rpm increases the powder feed rate. The sensor is validated through a few meticulously designed prints. To obtain the characteristic curve, a series of single tracks at different working distances are printed, the parameters will be specified later in CHAPTER 4. G-code and other parameters are obtained taking into account the prints feature, the powder material, and using previous knowledge acquired using the machine.

1.4 Keyence VR-6000

VR-6000 is a Keyence 3D measurement system that provides fast and high precision profilometry measurements. Its advanced scanning principle such as the HDR scanning algorithm enables automatic measurement in a wide range. The optimal scan settings are configured automatically ensuring accuracy in the measure for all sort of different features. Moreover, the VR system automatically recognizes the width and height of the target to automatically set the optimal measurement range, and the motorized stage automatically moves to scan the different sections of the object. The profilometer comes with software with abundant assistance tools and user-friendly measurement functions to help extract all sorts of data from the scan. The VR-6000 is equipped with an advanced optical design that allows us to acquire high precision and high-definition measurement data at both low and high magnifications. Two transmitter lenses placed at an angle with respect to the vertical direction generate a structured light that is then detected by the receiver lens and will appear banded and bent based on changes in the topography of the surface. Triangulation is then used to calculate and measure the height of the surface. A high-definition CMOS is adopted to acquire low noise data across the entire field of flow. RGB data is acquired for each pixel, providing excellent color imaging for surface inspection. To enable high accuracy measurements throughout the field of view, the VR Series uses a telecentric lens with extremely low lens aberration. Objects can be captured as they appear and at their actual size, ensuring high measurement accuracy anywhere on the screen. A total of three large aperture high resolution lenses are mounted on the transmitter and receiver parts. The system can scan objects with a resolution up to 0.1μm. The features of the system make it easy to directly scan an entire build plate with different prints on top, thereby it is used in the calibration process to measure the height of the single tracks.

CHAPTER 3 SENSOR HARDWARE DESIGN

The sensor system is divided in two parts: an acquisition optics and processing optics as shown in Figure 3. The former includes a focusing biconvex lens (I) that is originally part of the Optomec optical system that delivers/focuses the high intensity laser lights to the printing point to build the layer. This work uses this lens to collect and transmit the lights from the melt pool to the second focusing lens (II) that focuses the lights onto the aperture of the fiber optic cable. The processing optics collimates and filters the light from the fiber optic into two radiation bands which are then detected by two independent detectors. The filtered intensity data is saved by a computer.

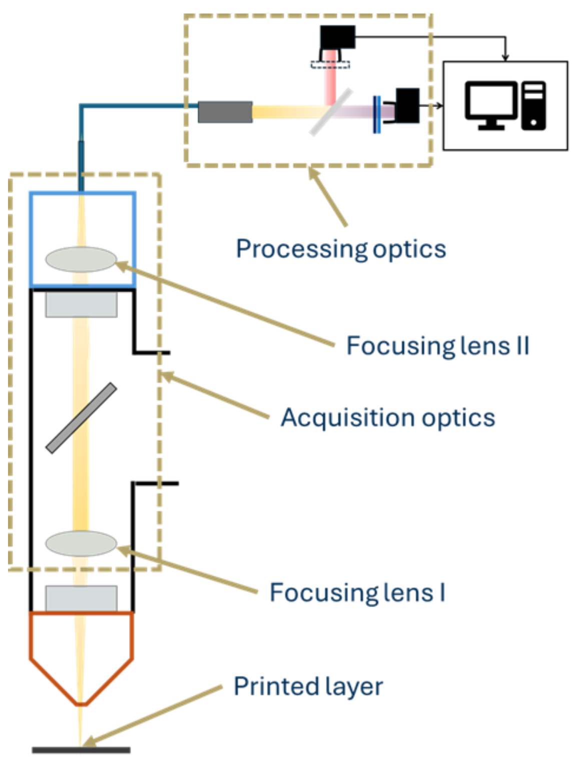

Figure 3 A schematic of the working distance measurement sensor

1.5 Radiation acquisition optics

Following the chromatic aberration technique presented in [15], an optical sensor is designed. The first part of the sensor is the radiation acquisition system responsible for collecting the radiation from the melt pool and delivering it to the optical detection box using a fiber optic.

1.5.1 Theory

Due to the nature of the sensor, the use of a ray tracing technique is necessary to model and understand the behaviour of the radiation generated. The easiest way to model a generical symmetric laser beam in two-dimensional space is to use a two-components column array. The first component represents the distance between the laser beam and the symmetry axis (x_0) while the second represents the angle between the two (θ_0) as shown in Figure 4.

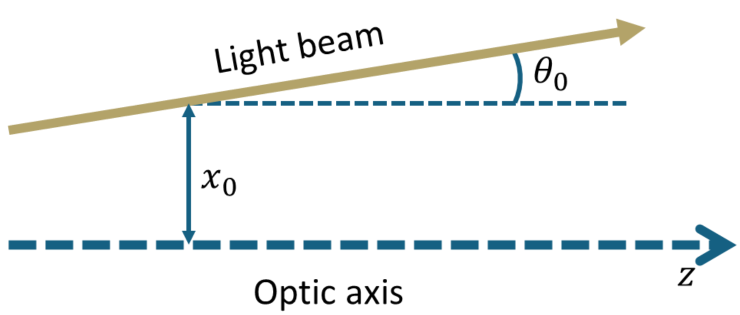

Figure 4 2-D laser beam representation scheme

Using this representation of laser beam information at a specific point, it is possible to trace its propagation in space and interaction with optical components such as lenses using multiplication of the transfer matrices. For example, the transfer matrix for the propagation in free space is the structure $P = \begin{bmatrix} 1 & z \\ 0 & 1 \end{bmatrix}$, where z is the distance of propagation and that for a lens is $L = \begin{bmatrix} 1 & 0 \\ -\frac{1}{f} & 1 \end{bmatrix}$, where f is its focal length.

Under the assumption of a thin lens, i.e. reasonably thin compared to the travel distances as in this analysis, it is possible to use an equation that relates the material property (the refractive index) and geometrical properties of the lens with its focal length f (Eq.2). Letting the refractive index of the lens material be a function of the wavelength $n(\lambda)$, the equation allows, for every lens, to calculate the focal length for each wavelength using (Eq.2), with the geometrical parameters shown in Figure 5.

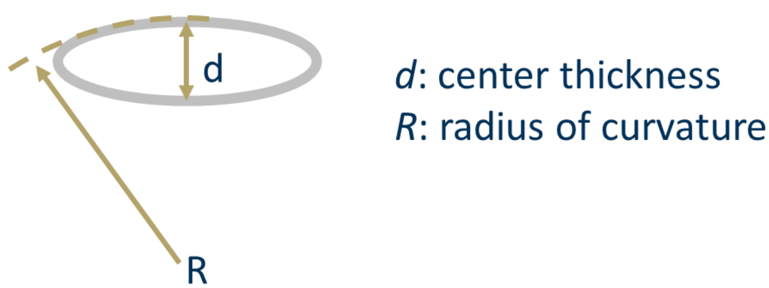

Figure 5 Thin lens scheme

$$\frac{1}{f} = (n-1)\left[\frac{2}{R} - \frac{(n-1)d}{nR^2}\right] \quad \text{(Eq.2)}$$

Finally, to complete the analysis on how the hot mirror inside the printing head interacts with the incoming light, Snell's law (Eq.3) (Eq.3)is used. Snell's law describes the relationship between the angle of incidence and the angle of refraction of a light beam passing through a boundary between two different isotropic media as shown in Figure 6.

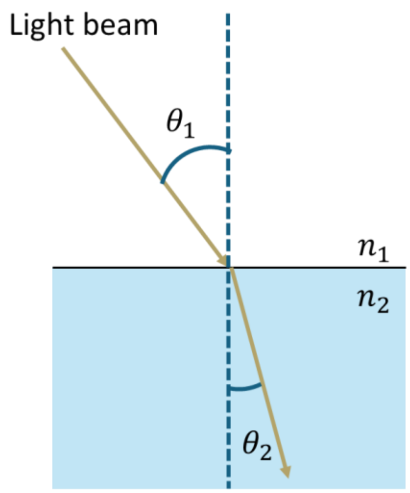

Figure 6 Snell's law

$$\frac{sin\theta_1}{sin\theta_2} = \frac{n_2}{n_1} \quad \text{(Eq.3)}$$

1.5.2 Optical scheme

First, the camera lens on top of the optical path in the printing head Figure 2, which seems to be installed by the manufacturer for possible uses with an external camera, is removed. This allows us to install a new focusing lens in desired specifications using a fiber optic cable to complete the radiation acquisition optics. In the analysis, the effects of the cover glasses are assumed to be negligible. Moreover, for the moment, the effects of the hot mirror on the system are ignored. Using the optical scheme shown in Figure 7, it is possible to analyse the light propagation and get an estimation of the best relative positions between the focusing lens I and II (Z_1) and the focusing lens II and the fiber optic terminal (Z_2). A major constraint is the clear aperture opening dimension $CA = 17mm$ on top of the optical path inside the printing head that limits the area the light can pass through. We define the working distance to be the focal length of the Optomec® lens, which is set to be $W_d = 200mm$ by the manufacturer. Z_1 should be as low as possible, avoiding excessive travel distances of the light. In addition, Z_1 is limited by design constraints due to the presence of the external sensor housing that will be designed later. Being W_d and Z_1 known values, it is now easy, using the techniques described in the previous paragraph, having an estimation of Z_2.

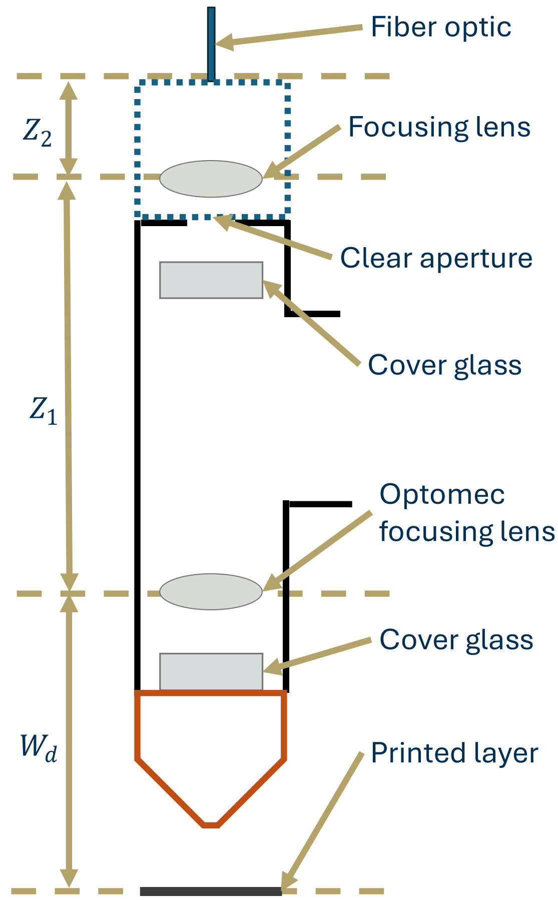

Figure 7 Sensor optical scheme

1.5.2.1 Detailed math

Following the scheme in Figure 7, the detailed calculations are presented here to reach the results. The instant before hitting the Optomec© focusing lens (or equivalently the focusing lens I) is taken as the starting point of the radiation beam Figure 8. Because the radius of the clear aperture is given $x_0 = 8.5mm$, only this extent of the focusing lens is considered. Light outside this range will not be detected by the detection fiber optics. By the geometry in Figure 8,

$$\theta_0 = \text{atan}\,(\frac{x_0}{W_d})$$

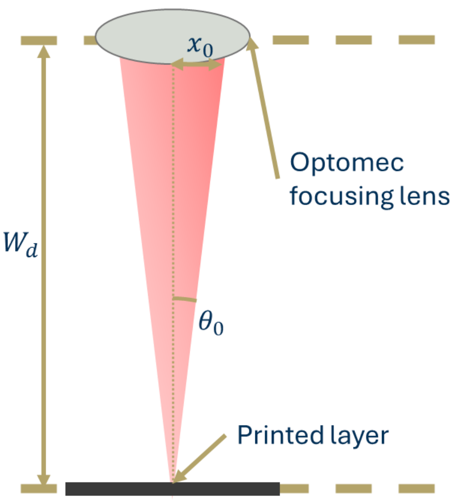

Figure 8 Radiation beam starting point

Now to track the acquired lights, for each single wavelength, until the fiber optic is reached, the following transfer matrices are sequentially multiplied:

$$L_1 = \begin{bmatrix} 1 & 0 \\ -\frac{1}{f_1(\lambda)} & 0 \end{bmatrix},\ L_2 = \begin{bmatrix} 1 & 0 \\ -\frac{1}{f_2(\lambda)} & 0 \end{bmatrix},\ P_1 = \begin{bmatrix} 1 & Z_1 \\ 0 & 1 \end{bmatrix}, \text{ and } P_2 = \begin{bmatrix} 1 & Z_2 \\ 0 & 1 \end{bmatrix}$$

to obtain $\begin{bmatrix} x_f \\ \theta_f \end{bmatrix} = P_2 L_2 P_1 L_1 \begin{bmatrix} x_0 \\ \theta_0 \end{bmatrix}$,

where L_1 and L_2 are the transfer matrices of the focusing lens I and II, respectively, and P_1 and P_2 are those of the propagation paths Z_1 and Z_2. Now an optimization problem is defined as follows: find Z_2 value that produces a smallest focal spot x_f for the wavelengths in the considered spectral band.

1.5.3 Acquisition optics elements

First, it is necessary to select a fiber optic cable. Due to the necessity of acquiring radiation on a wide range of wavelengths, a multimode cable is selected. The most important parameter is the numerical aperture (NA) (Eq.4) (Eq.4)(Eq.4)(Eq.4)(Eq.4), a ratio value measuring the maximum angle which allows the incident lights to enter the fiber optic cable interior as shown in Figure 9. A small NA leads to a low level of radiation acquired while a too high value leads to problem such as scattering inside the fiber optic, NA=0.39 is chosen as a good compromise.

$$NA = n_{air} sin(\theta_{acc}) = \sqrt{n_{core}^2 - n_{clad}^2} \tag{Eq.4}$$

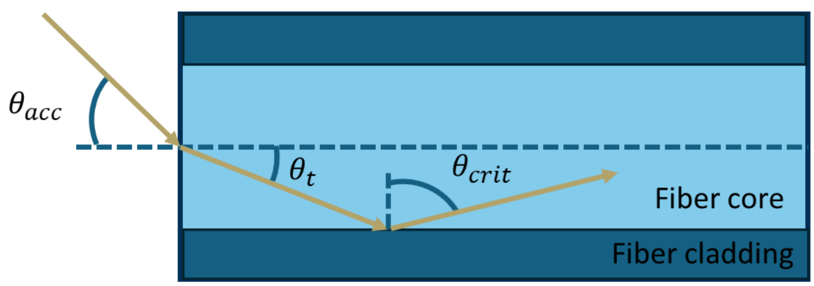

Figure 9 Fiber optic and NA

Table 2 Fiber optic specification

Wavelength range	400-2200nm
Numerical aperture	0.39
Core diameter	200μm

Now it is necessary to select a focusing lens II. To properly focus the light inside the fiber optic, a bi-convex lens is the best choice. Due to the necessity of collecting a wide range of wavelengths, a lens with no coating is appropriate. Among the available materials, NBK-7 is selected, considering its high transmission rate, $T_{avg} > 90\%$ in the wavelength range of interest. To enhance the effect generated by chromatic aberration the lights at different wavelengths should be focused at the highest angle possible, meaning the focal length should be as small as possible, maximizing the acceptance angle θ_{acc} (see Figure 10).

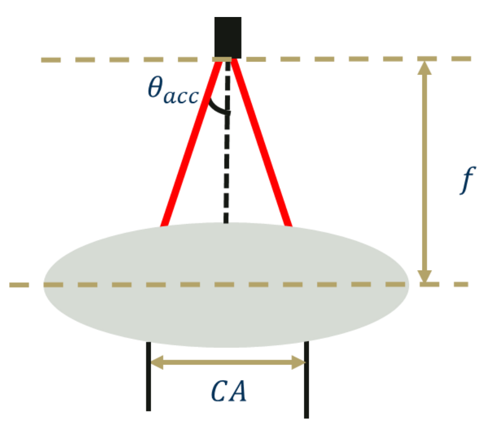

Figure 10 Lens selection

This brings 2 possible solutions, an approximately half inch diameter lens with $f = 15mm\ (0.59inch)$ and a one-inch diameter lens with $f = 25{,}4mm\ (1inch)$. Considering the width dimension of the clear aperture on the Optomec, the first lens allows a bigger acceptance angle while the second lens with a larger diameter allows a higher radiation detected. The half inch lens has an acceptance angle too big compared to the maximum allowed by the fiber optic $\theta_{acc\ 0.5inch} = 0.5 > \theta_{acc\ max} = 0.4$, leaving the one-inch lens as the best choice. Now using the data provided in Table 3 combined with the refractive index data [20], it is possible to calculate the focal length for each single wavelength using (Eq.2).

Table 3 Bi-convex sensor lens

Material	NBK-7
Diameter	1 inch
Focal length (at λ=587.6nm)	24.5 mm
Radius of curvature	24.5 mm
Center thickness	9 mm

The last element that needs to be analyzed is the Optomec© focusing lens based on the data available Table 1, plus the data on the refractive index of the fused silica [20]. To extract the data about the center thickness and the radius of curvature it is possible to look online for similar lenses and then adjust the value checking if the focal distance at 1080nm calculated with (Eq.2) matches the value in Table 1. The result is that a radius of curvature

$R = 179.33mm$ and a center thickness $d = 2.9mm$ give a focal length $f = 200.0049mm$ close enough to the value reported by the manufacturer.

1.5.4 Hot mirror analysis

The hot mirror inside the printing head reflects the path of the processing laser beam down toward the printing spot. The incoming lights from the printing layer will have to pass through this mirror before it is detected by the detection optics, by which the propagation paths will be modified due to the light refraction. Therefore, it is necessary to take this element into account for better focusing and detecting the incoming radiation. As we can see from Figure 11 the final effect is a shift of the focal point away from the symmetry axis of the laser beam. The question is how significant this shift will be. This is answered below.

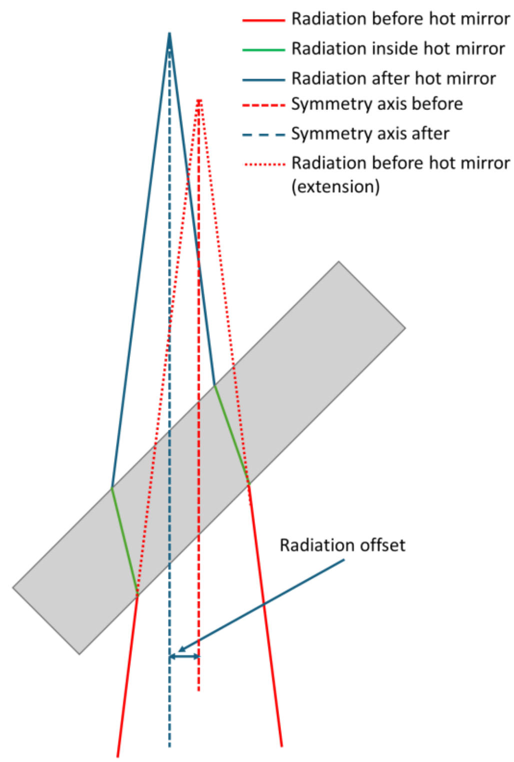

Figure 11 Refraction effect of hot mirror

Being the refractive index of the mirror bigger than the one of the Argon (the ambient medium of the optical system), i.e. $n_{mirror} > n_{Ar} \cong 1$, according to (Eq.3)(Eq.3), the focal point shifts to the left. To be able to provide an estimation on the dimension of this shift, it is necessary to know the refractive index and the thickness of the mirror. Because those parameters are unavailable as the manufacturer's proprietary information, the best way to deal with the problem is to analyse the worst-case scenario (the greatest shift possible) and make further decisions on optimization based on that. The worst-case scenario is given by the combination of highest refractive index with the highest mirror thickness. Being the refractive index decreasing when the wavelength increases, the analysis is conducted using the highest refractive index in the range of interest, e.g. at 400 nm which is the lower boundary of the fiber optic cable wavelength range. Table 4 puts together a list of commercial hot mirrors available online. It is clear that the worst combination is given by a 5mm thick fused silica mirror which are the data to be used for the analysis.

Table 4 Hot mirrors available online

Manufacturer	Thickness	Material (refractive index at 400nm)
Thorlabs©	5mm	Fused silica (1.47)
Thorlabs©	1mm	Soda-lime (1,53)
NewPort©	3,3mm	Borosilicate (1.53)
Abrisa©	1,1 / 1,75 / 3,3mm	Borosilicate (1.53)
Andover Corp©	3mm	Borosilicate (1.53)
Tower Optical©	3,3mm	Borosilicate (1.53)
EdmundOptics©	1,1 / 3,3mm	Borosilicate (1.53)

1.5.4.1 Detailed math

For what concerns the hot mirror using Figure 12 and the calculation below, we obtain an estimation of the offset with respect to the symmetry axis.

$$\theta_m = \frac{\pi}{4}, n_1 = 1, \ n_2 = 1.47, w = 5mm$$

$$\theta_1 = \theta_m + |\theta_{in}|, \theta_2 = asin\left(\frac{n_1}{n_2}\sin(\theta_1)\right)$$

$\overline{BC} = w \tan(\theta_2),\ \overline{AC} = w \tan(\theta_1),\ \overline{AB} = \overline{AC} - \overline{BC}$

$\overline{AD} = \overline{AB}\sin(\theta_m) - (\overline{AB}\sin(\theta_m))\tan(\theta_{in})$

$\theta'_1 = \theta_m - |\theta_{in}|, \quad \theta'_2 = asin\left(\frac{n_1}{n_2}\sin(\theta'_1)\right)$

$\overline{B'C'} = w \tan(\theta'_2),\ \overline{A'C'} = w \tan(\theta'_1),\ \overline{A'B'} = \overline{A'C'} - \overline{B'C'}$

$\overline{A'D'} = \overline{A'B'}\sin(\theta_m) - \left(\overline{A'B'}\sin(\theta_m)\right)\tan(\theta_{in})$

$offset = \overline{A'D'} + \frac{\overline{AD} - \overline{A'D'}}{2}$ =1.59 mm

Note that this amount is not negligible in the overall geometrical design of the optical system.

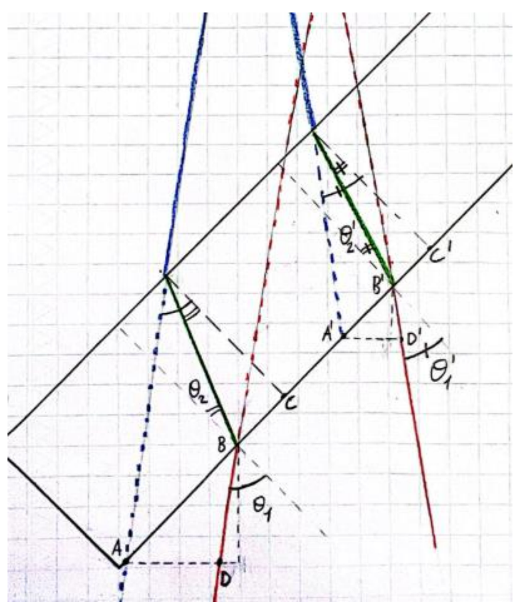

Figure 12 Hot mirror scheme

1.6 Processing optics

This second part of the sensor selects two specific spectral bands by optically filtering the acquired lights. The voltage responses at these spectral bands will be used to generate a calibration curve.

1.6.1 Radiation theory

To design the processing optics, it is important to understand the type of radiation that the melt pool generates. The source of radiation that we are focusing on is the melt pool which emits in a broad spectral band including both the visible and the IR lights. According to Plank's law of blackbody radiation [21], the spectral energy density of radiation emitted from a blackbody (an idealized physical body that absorbs all incident electromagnetic radiation) is a function of the temperature of the blackbody and the wavelength (Eq.5), where $h = 6.63 * 10^{-34} \frac{J}{Hz}$ is the Planck's constant, $c = 3 * 10^{8} \frac{m}{s}$ is the speed of light $k_b = 1.38 * 10^{-23} \frac{J}{K}$ is the Boltzmann's constant, T is the temperature of the body in Kelvin (K) and λ is the wavelength at which the energy density is emitted.

$$R(\lambda, T) = \frac{2hc^2}{\lambda^5} \frac{1}{e^{hc/k_b \lambda T} - 1} \quad \text{(Eq.5)}$$

In this paragraph the analysis would be limited to the materials to be used to evaluate the developed sensor, i.e. aluminum and steel. We assume that in standard conditions the temperature of the melt pool would be equal to the melting temperature of the single materials $T_{Al} = 933{,}5\ K, T_{Fe} = 1811K$. Now is possible to plot (Eq.5) for different values of λ as shown in Figure 13.

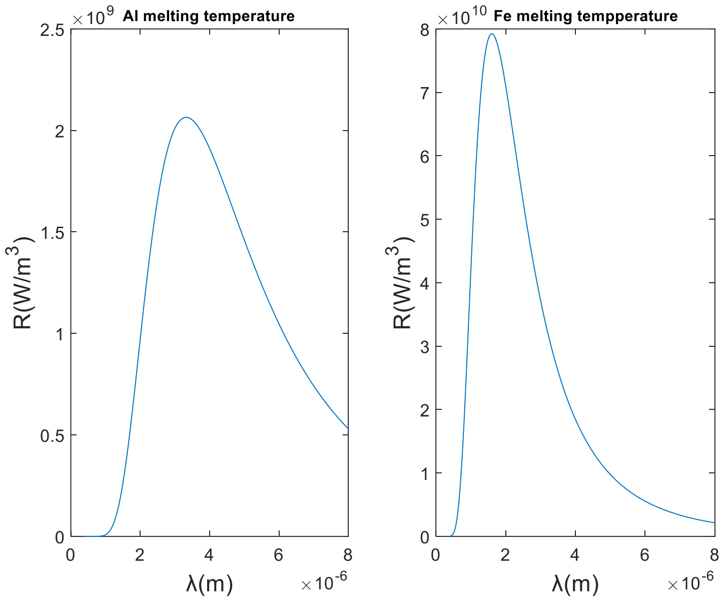

Figure 13 Radiation spectrum for aluminum and steel. Ideal Plank's blackbody radiation is assumed at their melting temperature

1.6.2 Components in processing optics

Since the effect of the chromatic aberration is bigger if the selected spectral bands are far from each other, to increase the sensitivity it is important to select the spectral bands apart as far as possible. In addition, it is important to take into account that as the hot mirror inside the printing head shields most of the IR radiation, the intensity detected in the IR spectrum will be significantly reduced. The optical system designed is shown in Figure 14. First, the light collected by the acquisition optics is shined out of the fiber optic using a multimode collimator that is creating a parallel light beam. A hot mirror ($R_{avg} > 97\%$ from 710 to 1200 nm) is placed to split the radiation into two spectral bands. The reflected IR lights are sent towards an InGaAs detector that covers wavelengths between 800-1700 nm. Moreover, a 1200 nm cut-off filter is placed also in front of the IR detector to avoid detection of low intensity higher infrared wavelengths. Therefore, the spectral band is equal to 800-1200nm respectively lower boundary of the InGaAs detector and cut off frequency of the filter. In case tests while printing will show a sufficiently high radiation detected, additional filters will be applied as needed to shrink the spectral band. The rest of the radiation transmitted through the hot mirror reach a silicon detector with wavelength range between 320-1100 nm. Since the intensity detected in this wavelength range is expected to be sufficiently high, a couple of filters are placed in front of the detector. A cut-on filter at 400 nm and a cut-off filter at 450 nm, will result in a spectral band 50 nm wide. The voltage outputs from both detectors are sent to a DAQ and then saved on a computer for further analysis.

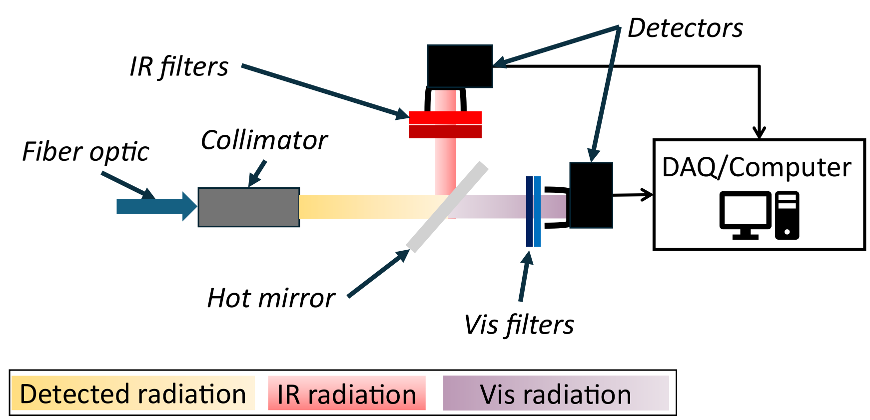

Figure 14 Optical detection box scheme

1.6.3 Radiation analysis

For each material we can focus our analysis on the spectral bands that we are interested in according to the filters selected for the processing optics. To consider the effects of the hot mirror inside the printing head for all the energy density of radiation at wavelengths higher than 700 nm, we assume the transmittance coefficient of 1% of the total radiation emitted as shown in Figure 15. Due to the wide range of values on the y axis, a plot on a log scale is shown in Figure 16.

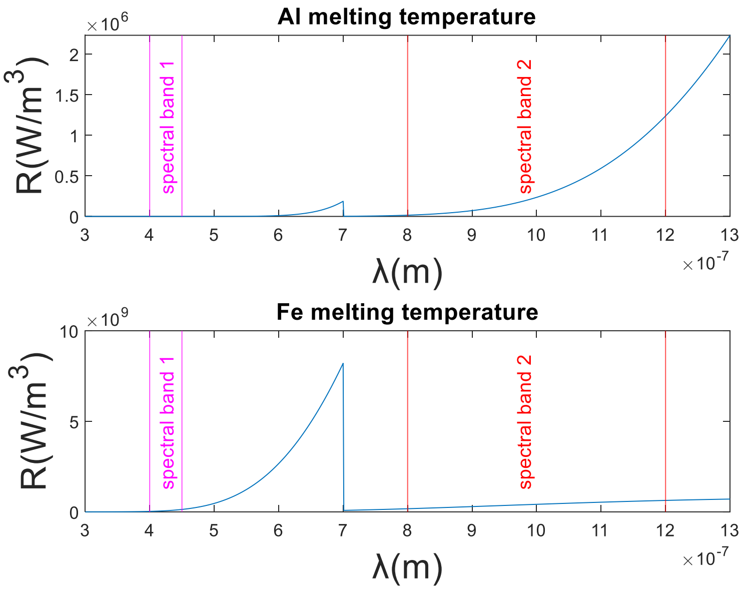

Figure 15 Theoretical radiation acquired by the sensor

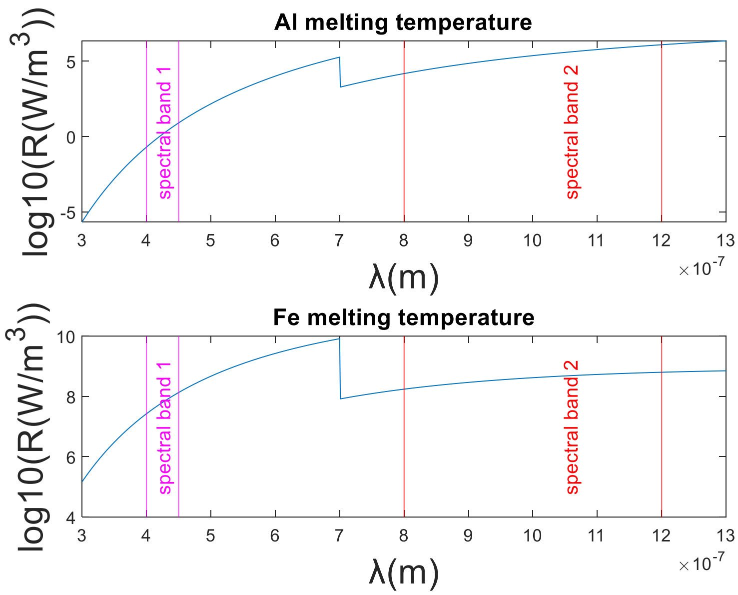

Figure 16 Theoretical radiation acquired by the sensor (log scale)

To evaluate the amount of intensity that we are expecting to get from each sensor we then integrate over the individual ranges of wavelengths for each detector as in (Eq.6) and (Eq.7). Then we define ν as the ration between the two detector outputs (Eq.8).

$$r_{vis} = \int_{450nm}^{400nm} R(T,\lambda)\, d\lambda \qquad \text{(Eq.6)}$$

$$r_{ir} = 0.01 \int_{1200nm}^{800nm} R(T,\lambda)\, d\lambda \qquad \text{(Eq.7)}$$

$$\nu = \frac{r_{ir}}{r_{vis}} \qquad \text{(Eq.8)}$$

For the aluminum $\nu_{Al} \approx 1.28 * 10^6$ and for the steel $\nu_{Fe} \approx 1.1 * 10^6$. In a real case scenario, the radiation emitted is lower than the one obtained by the blackbody radiation theory, and thus the two quantities are related by a factor called emissivity ε (Eq.9). The emissivity varies with the wavelength and with the temperature [22] but there is no mathematical equation to define the parameter in our range of interest. Further considerations could not be made without acquiring information on the emissivity in real time during the prints.

$$R_{real}(\lambda, T) = \varepsilon(\lambda, T) * R(\lambda, T) \quad \text{(Eq.9)}$$

The other main source of radiation to consider is the printing laser that has a wavelength of 1070nm, part of this radiation will be reflected from the melt pool and acquired by the sensor. Being a different type of radiation source, that could possibly interfere with the functioning of the sensor, a notch filter (CWL=1064 nm, FWHM=44 nm) is placed in front the IR detector to avoid the acquisition of this specific wavelength. Moreover, a 1200nm cut-off filter is placed also in front of the IR detector to avoid detection of low intensity infrared wavelengths longer than 1200nm (upper limit for the IR detector).

1.7 Design optimization

1.7.1 Trial tests

A copy of the Optomec® printing head is mounted on a vertical support as shown in Figure 17 to conduct test outside before the integration of the sensor on the actual

Optomec® printer. Now it is possible to place different radiation sources under the nozzle and analyse the voltage detected. To see if the overall system is working and it is able to process both visible and IR lights, two tests are conducted using two different radiation sources. For these initial tests both the lens and the terminal of the fiber optic cable are mounted on a Thorlabs® cage system and attached on top of the printing head using a cylinder support. To test the visible lights, a simple flashlight is used, while a piece of steel heated up to 1200°C (2192°F) using a furnace is used for the IR lights. The output voltages from the detectors are shown in Figure 18 and Figure 19. Figure 18 shows that the output signals in both IR and visible detectors clearly respond to turn-on and -off of the flashlight. Likewise, Figure 19 shows similar synchronous reaction of the detector to the IR lights form the hot steel plate. In this case, the signal magnitude decreases with time as the plate cools down. Those two tests demonstrate that the sensor can detect radiation both in the visible and the IR spectrum.

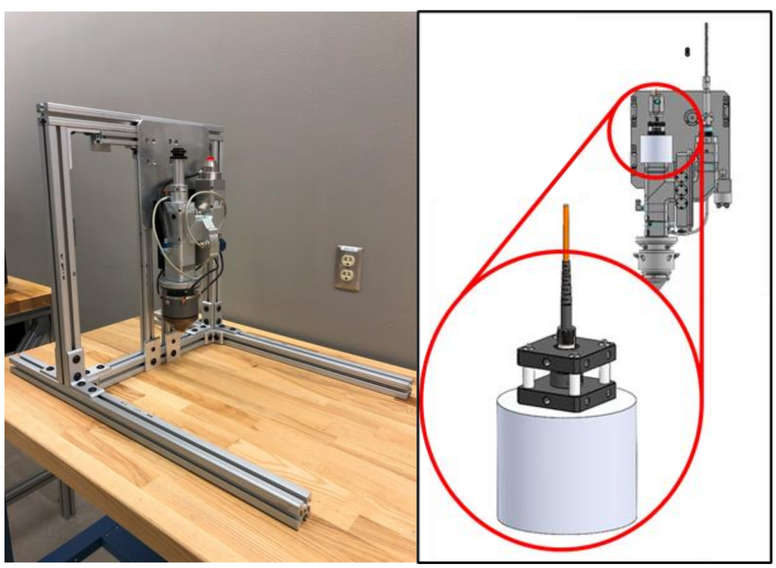

Figure 17 Optomec printing head on vertical support + first tests set-up

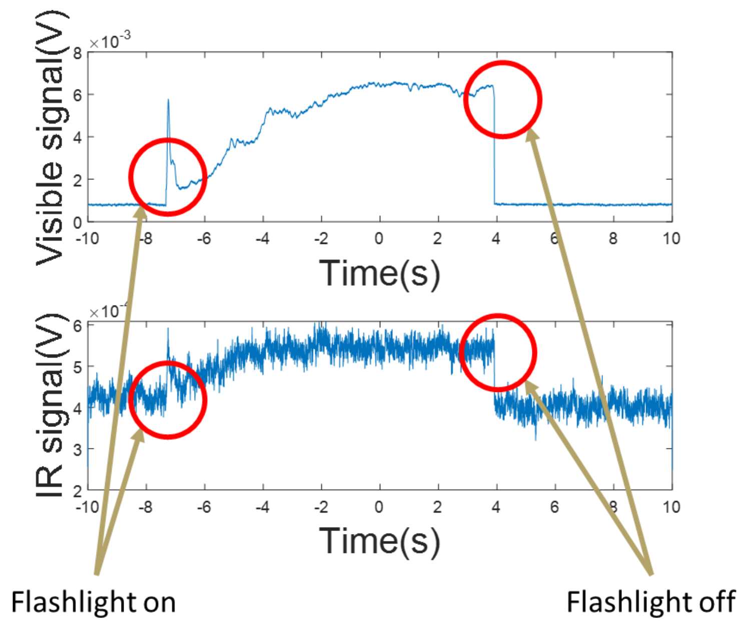

Figure 18 Sensor signa from the test with a flashlight

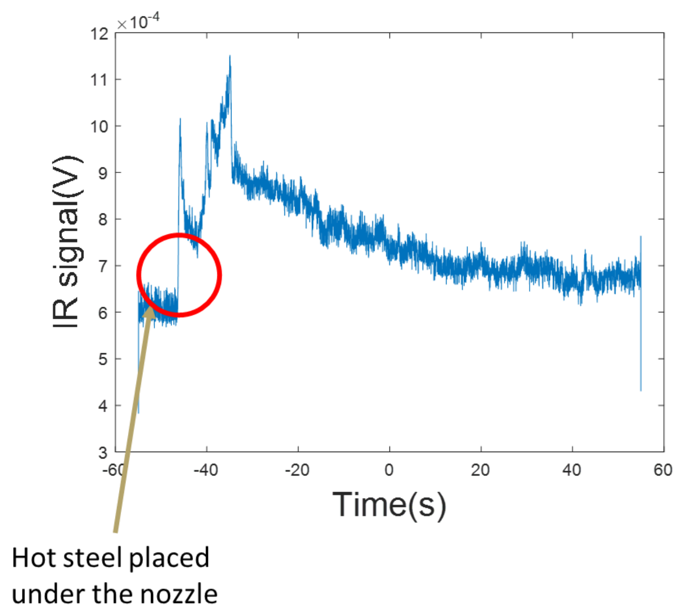

Figure 19 Sensor signa from the test with hot steel

1.7.2 Optimization setup and results

Following the analysis conducted in 1.5, the radiation acquisition system needs to be optimized. The best distance Z_2 and the best offset distance with respect to the symmetry axis need to be evaluated through some tests. The objective of the optimization is to maximise the voltage signal amplitude acquired by the detectors. The optimization set-up has three main parts Figure 20. A lens tube with internal thread is used to place and move precisely the focusing lens II and the fiber optic plate adapter. An X-Y motion stage is used to move the lens tube and adjust in the transverse direction. An additional piece to place on the bottom is designed to attach the entire system to the Optomec®.

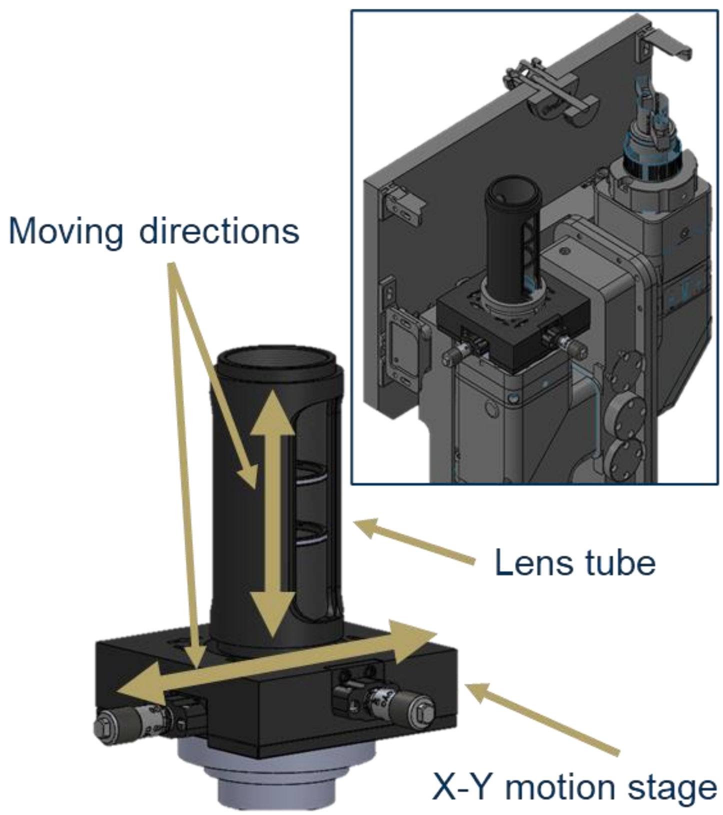

Figure 20 Optimization set-up

The result of Z_2 optimization is illustrated in Figure 21; the output voltage is maximized at the optimal value, $Z_2 = 1.013inch$. Now that $Z_1 = 6.087\ inch$ is fixed by the testing set-up we can compare the optimization result with the result provided by the theory analysis in 1.5.2. As a reference, the wavelengths at the center of each spectral band are taken for the analysis ($\lambda_{Vis} = 425nm$; $\lambda_{IR} = 1000nm$). The results are $x_{f\ Vis} = -0.3608mm$ and $x_{f\ IR} = 0.0034\ mm$, both values are close to zero showing the reliability of the tests results compared to the theory calculation.

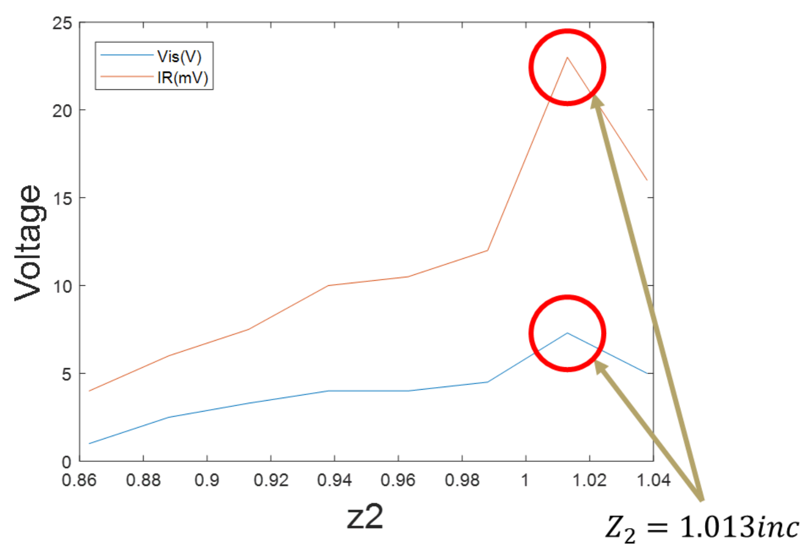

Figure 21 Z_2 optimal value

As predicted by the theory, placing an offset to the acquisition system with respect to the symmetry axis increases the voltage detected. As the sensor moves to the left, we can see the voltage increase, reaching a maximum value when the offset is equal to 1.25 mm as shown in Figure 22. The difference with the worst-case scenario, offset=1.59 mm calculated in 1.5.4 can be attributed to errors in the assumptions, particularly in an overestimation of the thickness of the hot mirror, while these two offset values are reasonably close to each other.

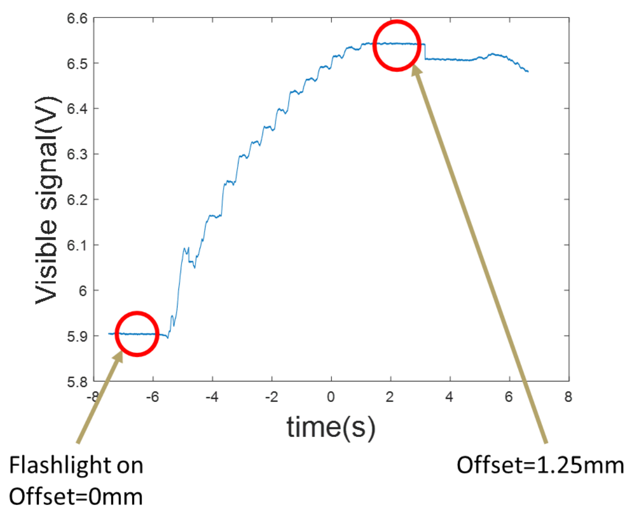

Figure 22 Transverse adjustment

1.7.3 Discussion on other sources of errors

The assumptions in the design process could leave some loss of signal outside of the analysis. Examples include the light that is reflected by the walls of the optical path inside the printing head, and the loss of signal and the small refraction due to the presence of the cover glasses. These are all considered minor sources of error and will not degrade the overall functioning of the sensor. As also showed from the optimization tests there is still a good signal-to-noise ratio.

1.8 Final design

From the results of the optimization, the final design of the radiation acquisition optical system is reached as shown in Figure 23. The Z_2 optimal distance is kept within the lens tube hosting both the biconvex focusing lens and the fiber-plate adapter. The external cover is made by three pieces joined with threads; between those pieces there are two O-rings to guarantee powder sealing of the inner part with respect to the printer chamber. The bottom piece of the external cover is designed to place the lens tube with a left offset with respect to the symmetry axis that is exactly the one obtained in 1.7.2. Moreover, the bottom part is designed to be attached to the printing head thanks to a thread in the lower part and positioned thanks to a lateral lip to avoid rotations. The internal part of the bottom piece has a thread to attach the lens tube that is holding the bi-convex lens (focusing lens II) and the fiber adapter plate.

1.8.1 Fiber optic cable

Finally, a cord grip at the top that allows the fiber optic cable to exit the inner part, while keeping the system powder sealed. The fiber optic cable is then delivered to the optical detection box placed outside the printing chamber to avoid powder contamination. While for testing was used an on-stock fiber optic cable with core diameter of 200 µm, having the possibility to custom the final cable design a 1500µm core diameter cable is chosen to increase the light that can be delivered. In addition, a more solid external cover of the cable is chosen made by stainless steel with a plastic sheath.

1.8.2 O-ring selection

The selection of O-rings is made using an online calculator provided by Parker-Hannif Corporation©. We know that the sealing case needs to hold an axial external pressure applied by the argon gas inside the printing chamber. Moreover, we narrow the search to a silicone 60 durometer O-ring and, as an additional factor of safety and set 200°F (93°C) as the maximum operating temperature. Fitting those parameters with the dimension of the external case we obtain our desired O-ring with; dash number, 222; inner diameter, 1.484 inches; cross section, 0.139 inches. The calculator provides also all the dimension to design the groove to place the O-ring.

1.8.3 Temperature safety

To avoid any problems derived from overheating of the acquisition system, some temperature measures have been taken in the area where the system is mounted using a thermocouple. The results show that even during extended periods of printing, the temperature is stable around 30°C (86°F). This value is safe for all the elements of the acquisition system, so no further modifications to the radiation acquisition system are needed.

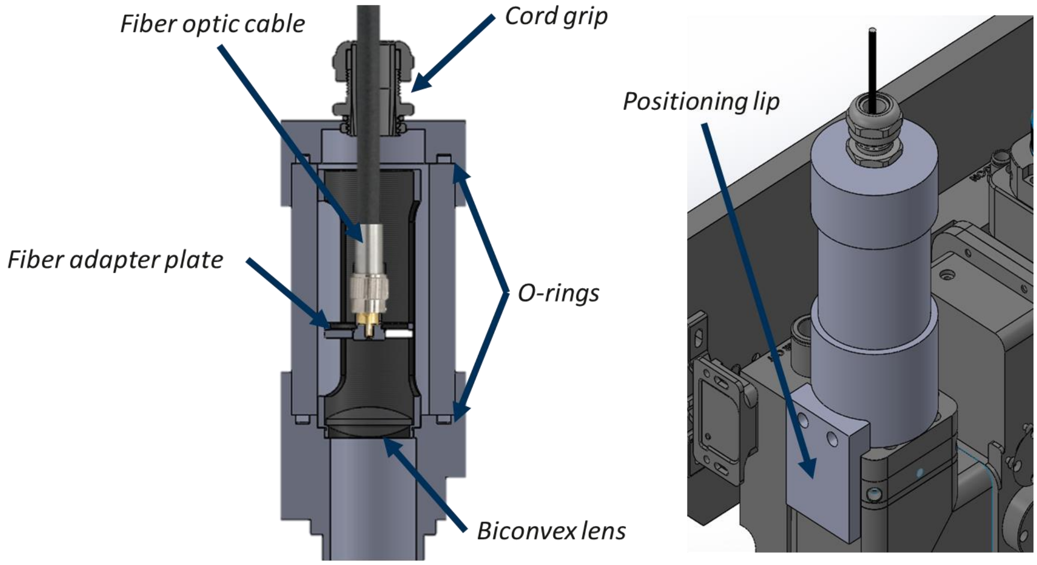

Figure 23 Final design

CHAPTER 4 SENSOR PERFORMANCE

1.9 Test description

In order to characterize the sensor performance, we need to build a calibration curve. The objective of the calibration curve is to have a plot showing a unique functional relation between a distance measure and the error signal defined in Eq.1. To get these data a series of single tracks are printed. Each test prints 75 different single tracks with 15 different standoff distances; the standoff distance means the distance between the build plate and the nozzle tip. The length of each track is 1 inch. The standoff distances are equally spaced between 0.2 and 0.312 inches with an increment of 0.008 inches between two of them. The range of distances chosen for the test is based on the focal point of the printing laser and the experience acquired through the use of the machine. A standoff distance smaller than 0.2 inches is too close to the build plate and the risk of physical interaction between the melt pool and the nozzle is too high; while all distances higher than 0.312 inches are too far from the build plate completely missing the focal point and resulting in almost no material deposited. During the entire process the sensor is turned on and is recording the data from the light emitted by the melt pool. After printing the Keyence VR-6000 profilometer is used to scan the tracks and extract the bead height measures. The test is repeated multiple times with the same parameters to ensure the repeatability and reliability of the sensor and to perform a statistical analysis on the calibration curve.

1.10 Stainless steel results

In Figure 24 are plotted the representative visible and IR voltage signals acquired during a test with 316 stainless steel for 75 different tracks as mentioned in the above paragraph. The printing parameters chosen to perform this test are: Laser Power, 450 W; Printing Speed, 20 inches/min; powder flow, 3 rpm. The sampling frequency is set at 5 kHz.

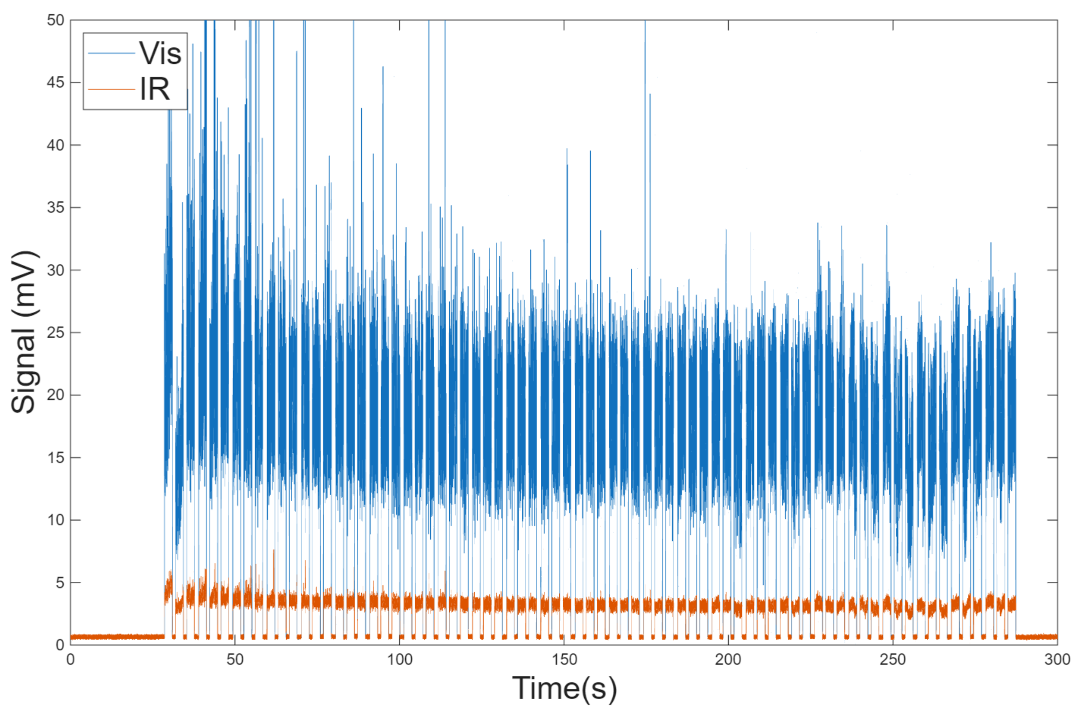

Figure 24 Visible and IR signals acquired during a test with stainless steel

As expected, the infrared signal is significantly reduced due to the presence of the hot mirror in the light path. Moreover, both the visible and IR signals largely fluctuate around certain levels for each test condition as shown in Figure 24. Both signals are then averaged over the time segment to obtain unique average levels for the two spectral bands. The working distance is evaluated simply subtracting for each track the bead height measured with the profilometer from the standoff distance set in the machine through the G-code, i.e. $Z_{wd} = Z_{stand-off} - Z_{bead}$. On the other hand, we can see that most of the signal is bounded between two values and only occasionally there are some points where the signal is detected out of these bounds. It is also interested to notice that usually local anomalies in the signal happens at the same moment in time in the two channels; this is due to unpredicted and random behaviour of the melt pool [23]. The phenomenon is particularly evident in the visible signal since the magnitude is higher than that in the infrared. Figure 25 shows the average levels of visible light for the repeated measurements. In this figure, it is seen that most of the data fall within the range 18mV and 25mV. Therefore, the data are processed such that the visible signal out of this range is discarded and the same for the infrared data.

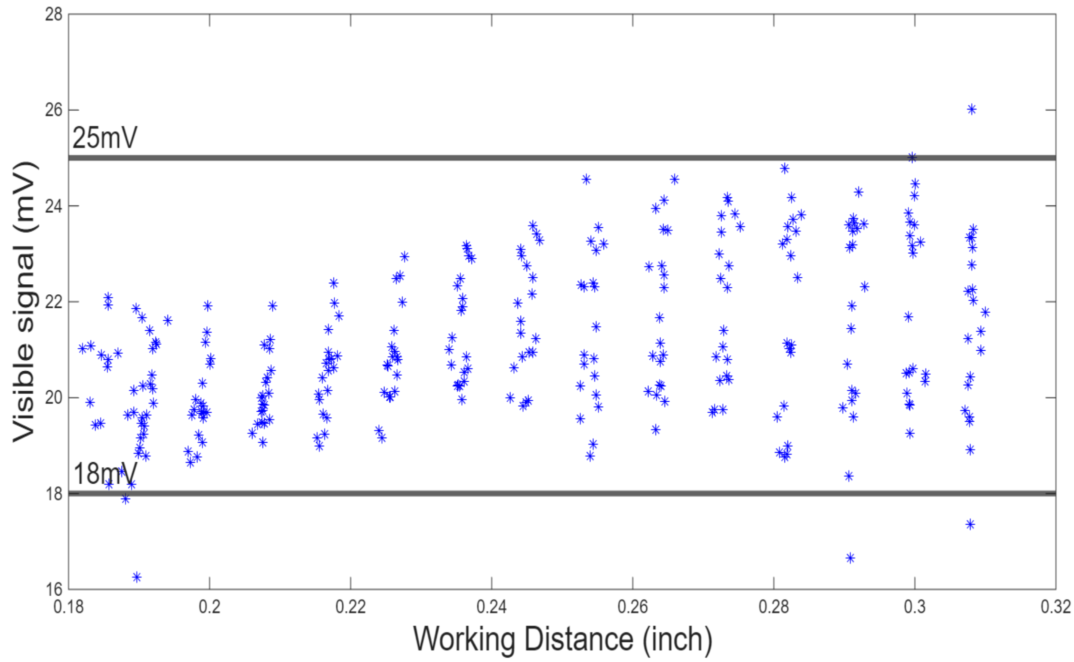

Figure 25 Visible voltage values plotted with respect to the working distance

The two voltage values are then combined using Eq.1, ensuring that the two terms (weighted signal) have similar orders of magnitude; the gain values are chosen as $G_{vis} = 1$ $G_{ir} = 5$. Now the statistical analysis is performed; data are divided into groups based on the standoff distance at which they have been acquired Figure 25. Being the deviation of the working distances for each standoff distance minimum, the mean working distance is taken as a representative value for further analysis. Figure 26 shows the mean error signal versus the working distance along with the standard deviation (σ and 2 σ). This plot constitutes the reference ε-W_d model for the real-time feedback control of the working distance.

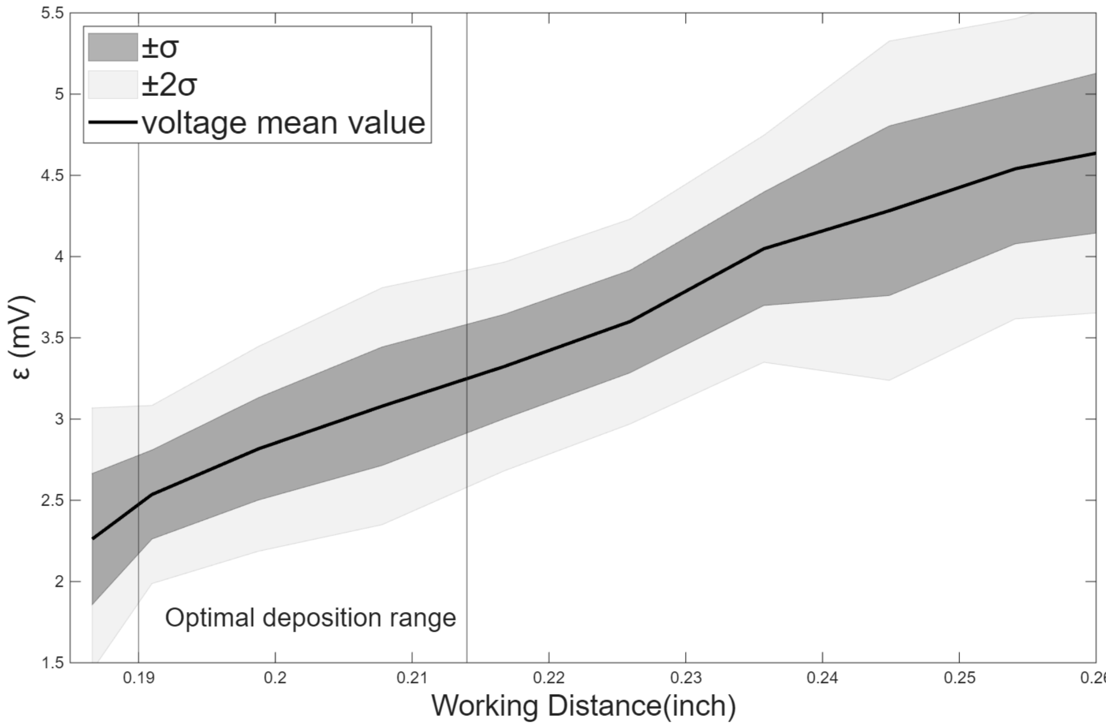

Figure 26 Calibration curve for stainless steel

1.11 Aluminum results

Since aluminium is more light-reflective than steel, sensor signal exhibit higher levels of noise. Trying to suppress excessive noise the IR bandwidth is reduced between 850 nm and 1100 nm. In Figure 27 are plotted the sensor signal from the two channels detected while printing A1000-RAM10. The parameters used for these tests are: Laser Power= 900 W, Printing Speed= 10 inch/min, Powder Flow= 3 rpm. Both the signals are lower than those from the stainless-steel test due to a lower melting temperature and consequently lower radiation emitted. In particular, the IR signal is very small because of the choice of the wavelength band. The voltage and the working distance values are calculated using the same process described for the steel. It is still possible to notice that, as in the stainless steel, most of the visible signal is clearly bounded within an upper and a lower limit. Again, looking at the plot of the mean levels of visible sensor signal in Figure 28, it is possible to clearly identify those boundaries at 1 mv and 8 mv.

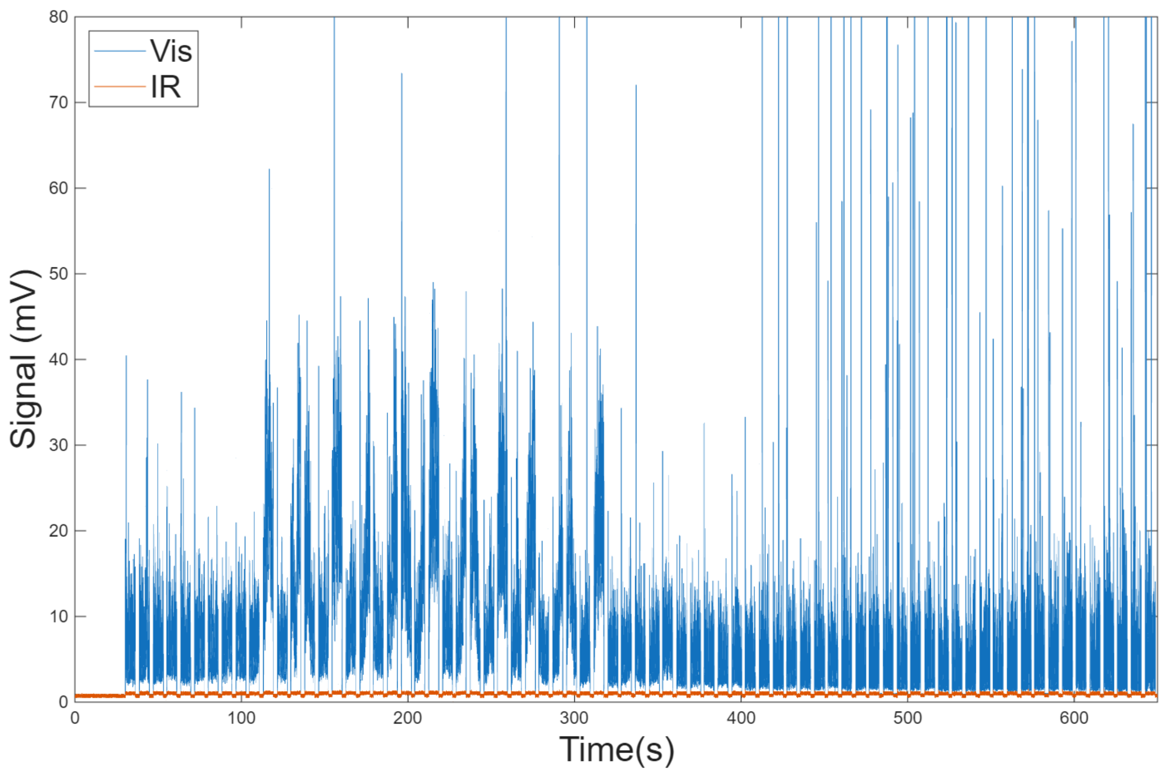

Figure 27 Data acquired during a test with aluminum

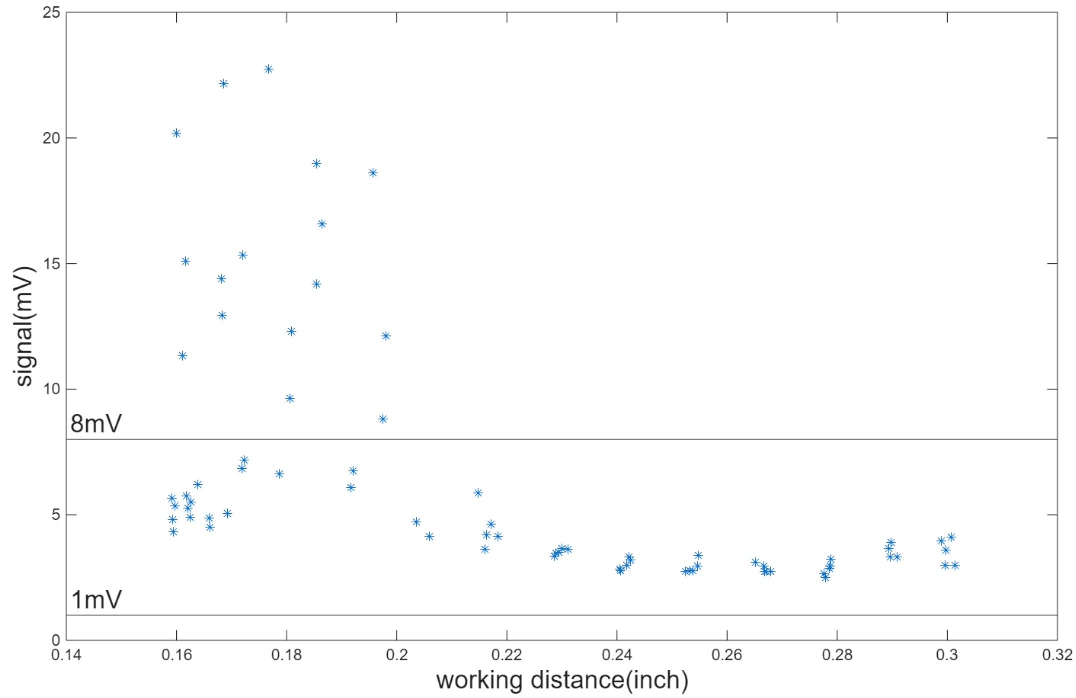

Figure 28 Average visible voltage levels plotted with respect to the working distance

The data are processed in the same way as for the stainless steel, the gains are selected to be $G_{vis} = 1$ $G_{ir} = 5$ considering the ratio between the two signals. Due to the low number of data available, only the mean line of the resulting values is plotted Figure 29.

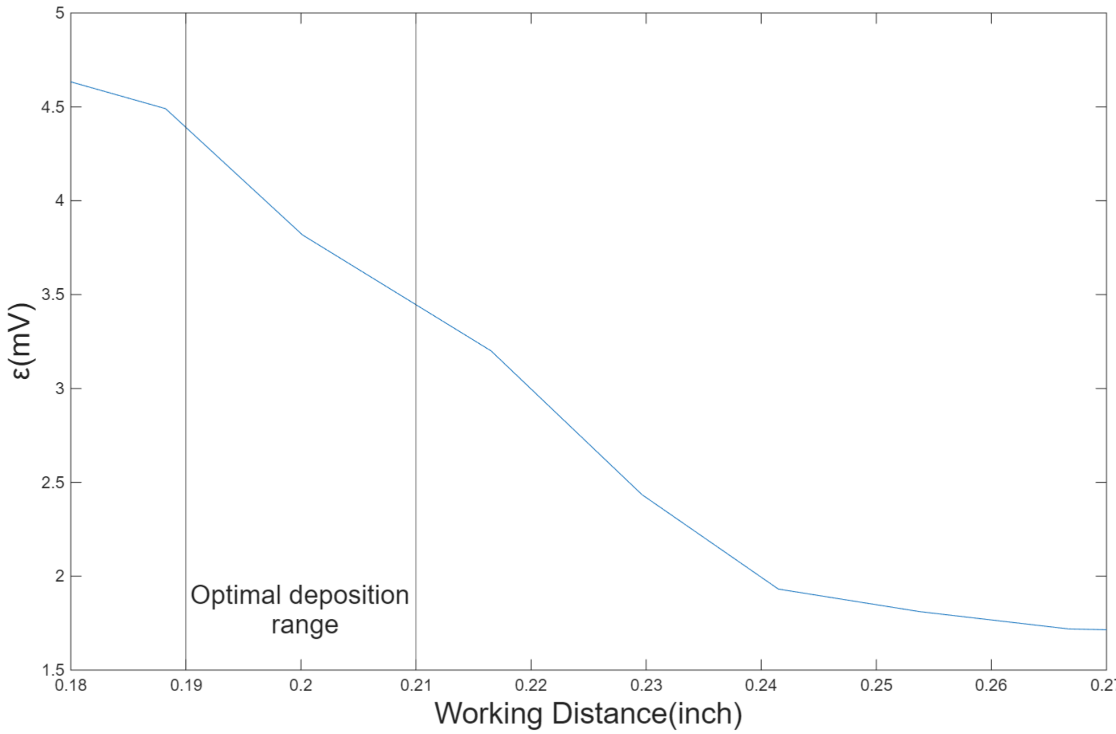

Figure 29 Calibration curve for aluminum

1.12 Discussion on the results

It is quite easy to distinguish between print and no print from sensor signals. The data acquired during the tests shows that the sensor can process the data generated by the data acquired during the printing process. Just from the raw data recorded it is possible to clearly distinguish the moments when the machine is printing and when the laser is off (there is a clear step in the sensor signal). For both the materials tested the calibration curves are monotonic in the range of interested (around the focal point of the laser) that contains the range of optimal deposition that corresponds to maximum track height. The monotonic behaviour is crucial to ensure the use of the sensor as a control during the printing process. The data acquired with stainless steel show that the data scatters are in an acceptable range. In particular, the standard deviation is minimal in the range corresponding to the maximum deposition. Further tests will help increase the confidence on the mean sensor signals measured by reducing the data scatter. The data acquired from printing with aluminium are not enough to make statistical considerations but, given the high reflectivity of the material, the monotonic behaviour of the obtained calibration curve is a promising result even with a material that tends to have a behaviour difficult to predict.

1.13 Additional tests

For a more accurate sensor calibration, the test proposed should be repeated multiple times with the purpose of enlarging the data set and reducing the deviation. Additional tests are needed for aluminum where only preliminary data have been acquired. Moreover, repeating the tests for varying parameters will underline how the calibration curve that is obtained for one specific parameter combination, is unique for each material and does not depend on the parameter choice. Different combinations of laser power and printing speed should be chosen trying to reach still good deposition rates and demonstrate that the calibration curve is unique to each material, independent from the specific choice of printing parameters. In Table 5 and Table 6 some possible combinations of parameters are proposed. Due to the fluctuation of the powder flow [24] and not being able to track its change over time, the rpm set on the powder hopper is kept constant in this analysis.

Table 5 New combinantion of parameters for stainless steel tests

	Laser Power (W)	Printing Speed (inch/min)
Original data	450	20
New data 1	400	15
New data 2	550	30
New data 3	500	25

Table 6 New combinantion of paramters for aluminum tests

	Laser Power (W)	Printing Speed (inch/min)
Original data	450	20
New data 1	400	15
New data 2	550	30
New data 3	500	25

CHAPTER 5 CONCLUSIONS AND FUTURE WORK

1.14 Real time feedback control

After completing the calibration process, the developed sensor is ready to be implemented for real time feedback control of working distance in the specific DED printing process carried out on the Optomec® machine. It is shown that the error signals as a weight subtraction of the two detectors signals (visible and IR) are directly correlated to a working distance. The use of detectors makes it possible to acquire data at a frequency higher than all camera-based applications, increasing the amount of distance measurements that is possible to calculate per unit of time. If the detected distance is away from the desired distance, there are two possible ways to act and compensate for the error. The first one is simply adjusting the nozzle vertical position to restore the desired distance and therefore the catching efficiency. This is the easiest action, and it is necessary in situation where the actual working distance is particularly far from the ideal one. Alternatively, it is possible to change the other printing parameters, in particular laser power and printing speed, to locally adjust the amount of material deposited to keep the overall deposition rate constant.

Being an emerging technology, research in DED is often conducted trying new parameter combinations, new geometries, or new alloys. Tests usually consist of a series of fast and small prints to generate samples for further analysis. In this process it is common that some of the samples printed fail for several reasons. The result is that the machine is trying to print parts that are heavily compromised, and the deposition of additional material is useless and, in some cases, impossible. As discussed earlier, the sensor is completely able to distinguish between situations when the material is deposited (a clear signal is detected) and situations where there is no melt pool and no material is deposited (almost completely absence of signal detected). This type of information is potentially useful to develop a decision-based algorithm to improve the efficiency in research. The algorithm will establish whether it is worth or not to print each single sample, completing the prints only of the samples that have not failed and can be analysed, saving time, energy and material.

In conclusion, the calibration curve evaluated for stainless steel in Figure 26 can already be useful to implement a first and preliminary control feedback. We know that the optimal deposition range corresponds to a sensor output between 2 and 4 mV. If the voltage in output appears to increase over 4 mV and be stable above this value during the printing process, this is directly correlated to an increase in the working distance. Based on the increase in the signal it is now possible to act and move the printing head accordingly to reduce the working distance. This simple and maybe little adjustments can limit the variation of the working distance within a range of values that, if small enough and carefully selected, can lead to a multi-layer print where the working distance is self-converging [8].

1.15 Applicability in DED technology

All the optical elements in the sensor are available in the market. Moreover, the number of elements added on the print head is minimal (only a focusing lens and a fiber plate adapter) making the sensor easily implemented in other printers with a similar optical configuration. For printing heads designed with a free optical channel in line with the deposition nozzle, such as the Optomec®, it is possible to follow a completely similar design. In case of designs where the printing laser is in line with the deposition nozzle, the use of a dichroic mirror [17] could be implemented to collect the melt pool radiation. Being able to redesign the head selecting the optical components considering the presence of a working distance sensor will improve the performance and optimize the space occupied by all the elements. Collecting the radiation into the fiber cable allows placing the processing optics in any desired location preventing powder contamination and making all those elements easy to access. In conclusion, the proposed sensor has multiple advantages with an easier and potentially way more compact setup.

1.16 Future work

The results in CHAPTER 4 are promising in showing the possible application of the developed sensor for real time feedback control of powder blown laser DED systems. To better prove the reliability of the sensor additional tests as proposed in the previous chapter can be made. Moreover, performing the test for different combinations of printing parameters will give a better picture on the range of applicability of the sensor. Although the entire system is already at an advanced prototype stage, multiple further investigations can still be done. The integration of the elements in the printing head can be optimized evaluating the possibility to place the sensor focusing lens inside the printing head, avoiding the design of a sensor case. Theoretically it is always possible to increase the effect of the chromatic aberration by reducing the bandwidths and placing the two band farther from each other, so different spectral bands can be tested changing the elements in the processing optics. Since the measure is based on the radiation emitted by the melt pool, that is different for each material, it could be possible to find a different combination of spectral bands that provides higher sensitivity for a given material. In addition, it is also possible to explore other methods of processing the data acquired. Exploring more complex data processing based on the physics of the process could help improve the sensor performances. A refined version of the sensor, together with a large number of data accumulated, can potentially be able to predict the calibration curve of a given alloy directly relating it to its blackbody radiation.

REFERENCES

[1] D.-G. Ahn, "Directed Energy Deposition (DED) Process: State of the Art," *International Journal of Precision Engineering and Manufacturing-Green Technology,* vol. 8, pp. 703-742, 2021, doi: 10.1007/s40684-020-00302-7.

[2] K. S. B. Ribeiro, H. H. L. Núñez, G. S. Venter, H. R. Doude, and R. T. Coelho, "A hybrid machine learning model for in-process estimation of printing distance in laser Directed Energy Deposition," *The International Journal of Advanced Manufacturing Technology,* vol. 127, pp. 3183-3194, 2023, doi: 10.1007/s00170-023-11582-z.

[3] R. Seede, D. Shoukr, B. Zhang, A. Whitt, S. Gibbons, P. Flater, A. Elwany, R. Arroyave, and I. Karaman, "An ultra-high strength martensitic steel fabricated using selective laser melting additive manufacturing: Densification, microstructure, and mechanical properties," *Acta materialia.,* vol. 186, pp. 199-214, 2020, doi: 10.1016/j.actamat.2019.12.037.

[4] W. Zhang, M. Soshi, and K. Yamazaki, "Development of an additive and subtractive hybrid manufacturing process planning strategy of planar surface for productivity and geometric accuracy," *The International Journal of Advanced Manufacturing Technology,* vol. 109, pp. 1479-1491, 2020, doi: 10.1007/s00170-020-05733-9.

[5] Y. Xiong, J. E. Smugeresky, and J. M. Schoenung, "The influence of working distance on laser deposited WC–Co," *Journal of materials processing technology,* vol. 209, pp. 4935-4941, 2009, doi: 10.1016/j.jmatprotec.2009.01.016.

[6] D.-S. Shim, G.-Y. Baek, J.-S. Seo, G.-Y. Shin, K.-P. Kim, and K.-Y. Lee, "Effect of layer thickness setting on deposition characteristics in direct energy deposition (DED) process," *Optics & laser technology.,* vol. 86, pp. 69-78, 2016, doi: 10.1016/j.optlastec.2016.07.001.

[7] M. W. Vaughan, M. Elverud, J. Ye, R. Seede, S. Gibbons, P. Flater, B. Gaskey, R. Arroyave, A. Elwany, and I. Karaman, "Development of a process optimization framework for fabricating fully dense advanced high strength steels using laser directed energy deposition," *Additive manufacturing.,* vol. 67, p. 103489, 2023, doi: 10.1016/j.addma.2023.103489.

[8] J. C. Haley, B. Zheng, U. S. Bertoli, A. D. Dupuy, J. M. Schoenung, and E. J. Lavernia, "Working distance passive stability in laser directed energy deposition

additive manufacturing," *Materials & design.,* vol. 161, pp. 86-94, 2019, doi: 10.1016/j.matdes.2018.11.021.

[9] A. Mozaffari, A. Fathi, A. Khajepour, and E. Toyserkani, "Optimal design of laser solid freeform fabrication system and real-time prediction of melt pool geometry using intelligent evolutionary algorithms," *Applied soft computing.,* vol. 13, pp. 1505-1519, 2013, doi: 10.1016/j.asoc.2012.05.031.

[10] T. G. Fleming, D. T. Rees, S. Marussi, T. Connolley, R. C. Atwood, M. A. Jones, J. M. Fraser, C. L. A. Leung, and P. D. Lee, "In situ correlative observation of humping-induced cracking in directed energy deposition of nickel-based superalloys," *Additive manufacturing.,* vol. 71, p. 103579, 2023, doi: 10.1016/j.addma.2023.103579.

[11] I. Jeon, L. Yang, K. Ryu, and H. Sohn, "Online melt pool depth estimation during directed energy deposition using coaxial infrared camera, laser line scanner, and artificial neural network," *Additive manufacturing.,* vol. 47, p. 102295, 2021, doi: 10.1016/j.addma.2021.102295.

[12] S. Donadello, M. Motta, A. G. Demir, and B. Previtali, "Monitoring of laser metal deposition height by means of coaxial laser triangulation," *Optics and Lasers in Engineering,* vol. 112, pp. 136-144, 2019, doi: 10.1016/j.optlaseng.2018.09.012.

[13] M. Kogel-Hollacher, S. André, T. Beck, M. B. North Morris, K. Creath, J. Burke, and A. D. Davies, "Low-coherence interferometry in laser processing: a new sensor approach heading for industrial applications," *Interferometry XIX,* p. 122, 2018, doi: 10.1117/12.2501295.

[14] M. Kogel-Hollacher, M. Strebel, C. Staudenmaier, H.-I. Schneider, D. Regulin, H. Helvajian, B. Gu, and H. Chen, "OCT sensor for layer height control in DED using SINUMERIK® controller," *Laser 3D Manufacturing VII,* p. 23, 2020, doi: 10.1117/12.2540167.

[15] D. P. Hand, M. D. T. Fox, F. M. Haran, C. Peters, S. A. Morgan, M. A. McLean, W. M. Steen, and J. D. C. Jones, "Optical focus control system for laser welding and direct casting," *Optics and lasers in engineering,* vol. 34, pp. 415-427, 2000, doi: 10.1016/S0143-8166(00)00084-1.

[16] M. Ćwikła, A. Zakrzewski, P. Koruba, P. Jurewicz, and J. Reiner, "Preliminary design of longitudinal chromatic aberration sensor implemented to laser processing head," in *Optics and Measurement International Conference 2019*, 2019, p. 3.

[17] C. Herberger, L. Heinrich, E. Laneave, B. Post, K. B. Fillingim, E. Macdonald, T. Feldhausen, and J. Haley, "Coaxial color channel focus evaluation to estimate standoff height in directed energy deposition additive manufacturing," *Progress in Additive Manufacturing,* vol. 9, pp. 2199-2211, 2024-12-01 2024, doi: 10.1007/s40964-024-00572-6.

[18] A. Wang, H. Wang, Y. Wu, and H. Wang, "3D printing of aluminum alloys using laser powder deposition: a review," *The International Journal of Advanced Manufacturing Technology,* vol. 116, pp. 1-37, 2021-09-01 2021, doi: 10.1007/s00170-021-07440-5.

[19] P. Guo, B. Zou, C. Huang, and H. Gao, "Study on microstructure, mechanical properties and machinability of efficiently additive manufactured AISI 316L stainless steel by high-power direct laser deposition," *Journal of materials processing technology,* vol. 240, pp. 12-22, 2017, doi: 10.1016/j.jmatprotec.2016.09.005.

[20] M. N. Polyanskiy, "Refractiveindex.info database of optical constants," *Scientific Data,* vol. 11, 2024-01-18 2024, doi: 10.1038/s41597-023-02898-2.

[21] G. S. Ranganath, "Black-body radiation," *Resonance,* vol. 13, pp. 115-133, 2008-02-01 2008, doi: 10.1007/s12045-008-0028-7.

[22] H. Watanabe, J. Ishii, H. Wakabayashi, T. Kumano, and L. Hanssen, *Spectral Emissivity Measurements* vol. 46. Amsterdam, The Netherlands :: Academic Press, 2014.

[23] M. Schmidt, K. Partes, H. Naesstroem, and J. Volpp, "Relating vapor emissions to melt pool behavior during laser processing," *Journal of Laser Applications,* vol. 36, 2024-11-01 2024, doi: 10.2351/7.0001591.

[24] F. S. H. B. Freeman, B. Thomas, L. Chechik, and I. Todd, "Multi-faceted monitoring of powder flow rate variability in directed energy deposition," *Additive manufacturing letters.,* vol. 2, p. 100024, 2022, doi: 10.1016/j.addlet.2021.100024.